Chinese Physics Letters

EXPRESS LETTER

Weak Volume–Surface Coupling as a Dynamic Descriptor of Efficient Cell Migration under Physical Confinement

Cite as: Mingxi Xie *et al*. 2026 *Chin. Phys. Lett.* **43** 060902

Recommended Articles

Characteristics of Speed–Acceleration Phase Diagram of Migrating Cells
Yikai Ma, and Wei Chen
Chin. Phys. Lett. **40**, (2023)

Pressure-Modulated Activation Energy as a Unified Descriptor of Mechanical Behavior in Metallic Glass
Huanrong Liu, Jian Li, Shan Zhang, and Pengfei Guan
Chin. Phys. Lett. **43**, 010602 (2026)

Physical Properties of RhGe and CoGe Single Crystals Synthesized under High Pressure
Shangjie Tian, Xiangjiang Dong, Bowen Zhang, Zhijun Tu, Runze Yu, Hechang Lei, and Shouguo Wang
Chin. Phys. Lett. **42**, 110708 (2025)

Ultrafast Modulation of the Molten Metal Surface Tension under Femtosecond Laser Irradiation
Chenhao Li, Hongtao Liang, Yang Yang, Zhiyong Yu, Xin Zhang, Xiangming Ma, Wenliang Lu, Zhenrong Sun, and Ya Cheng
Chin. Phys. Lett. **39**, 077901 (2022)

Carrier Dynamics and Enhanced Terahertz Generation in GaAs Photoconductive Emitters with Microstructures
Yanrong Xiang, Zuanming Jin, Lei Hou, Zhiqiang Lan, Yang Li, Yan Peng, and Yiming Zhu
Chin. Phys. Lett. **42**, 110403 (2025)

Non-Hermitian Physics in Mesoscopic Electron Transport Through Coupled Quantum Dots
Yiyang Li, Jincheng Lu, Chen Wang, and Jian-Hua Jiang
Chin. Phys. Lett. **42**, 047303 (2025)

A series journal of Chinese Physical Society distributed by IOP Publishing

Chinese Physics Letters

Chin. Phys. Lett. **43** 060902 (2026)

EXPRESS LETTER

DOI: 10.1088/0256-307X/43/6/060902
CSTR: 32039.14.0256-307X.43.6.060902

Weak Volume–Surface Coupling as a Dynamic Descriptor of Efficient Cell Migration under Physical Confinement

Mingxi Xie[1,2], Bingrui Sun[1,2], Teng Ye[3], Yuxue Shu[1,2], Ying Lu[1], Qihui Fan[1,*], Xiaochen Wang[1,*], and Fangfu Ye[1,2,4,5,*]

[1]Beijing National Laboratory for Condensed Matter Physics, Institute of Physics, Chinese Academy of Sciences, Beijing 100190, China
[2]School of Physical Sciences, University of Chinese Academy of Sciences, Beijing 100049, China
[3]Department of Orthopaedic Surgery, Shanghai Sixth People's Hospital Affiliated to Shanghai Jiao Tong University School of Medicine, Shanghai 200233, China
[4]Wenzhou Institute, University of Chinese Academy of Sciences, Wenzhou 325000, China
[5]Oujiang Laboratory (Zhejiang Lab for Regenerative Medicine, Vision and Brain Health), Wenzhou 325000, China

[*]Corresponding authors. Email: fanqh@iphy.ac.cn; xcwang@iphy.ac.cn; fye@iphy.ac.cn

Cancer cell invasion through physically confined spaces is governed by the biophysical interplay between morphological plasticity and mechanical constraints. A fundamental but unresolved question is how cells sustain efficient movement under such confinement without compromising their global volume homeostasis. Here, using a Matrigel-overlay quasi-three-dimensional system, we show that confinement-enhanced migration does not arise from static structural changes, but from a reorganization of volume–surface dynamics accompanied by changes in cellular mechanical state. To quantify this reorganization, we introduce a volume–surface dynamic correlation coefficient, C. This metric decreases significantly during confined migration, indicating a state of weak coupling between volume regulation and surface remodeling. Perturbations of processes essential for both motility and volume homeostasis consistently increase C, despite affecting cell behavior through distinct routes. Together, these findings identify weak volume–surface coupling as a dynamic descriptor of efficient migration under confinement.

Introduction

Cancer cell migration in vivo occurs in mechanically complex microenvironments, where cells experience spatial confinement together with cell–matrix interactions [1,2]. Under these conditions, efficient migration requires repeated cell deformation while preserving overall volume homeostasis [3,4]. However, how this enhanced migratory state is dynamically organized under confinement remains unclear.

A primary challenge in addressing this mechanism is that cell–matrix contacts in three-dimensional (3D) environments extend across the entire cell surface, making surface remodeling a central physical driver rather than a secondary geometric readout [5,6]. Consequently, migration is fundamentally shaped by the continuous deformation of the global cell boundary [7,8]. Recent studies suggest that changes in cell volume can remain dynamically coupled to surface deformation during cell-state transitions [9–12].

Despite this, the nature of the coupling between cell volume and surface deformation during persistent migration remains poorly understood. Most studies of cell volume have relied on static measurements or acute responses to external stress [13,14], which fail to capture the dynamic coordination between volume regulation and surface remodeling. Furthermore, traditional two-dimensional descriptors cannot adequately resolve the three-dimensional height variations and boundary dynamics inherent to confined motility [15].

To overcome these limitations, we employed a Matrigel-overlay quasi-3D migration system to perform a systematic quantitative study of confinement-enhanced migration. Our study demonstrates that confinement-enhanced migration is not accompanied by detectable changes in static cell geometry, but is associated with changes in cellular mechanical state and a reorganization of volume–surface dynamics. This shift is well captured by a new metric for the coordination between volume regulation and surface remodeling, C, which identifies weak volume–surface coupling as a dynamic descriptor of efficient migration under confinement.

Results

Confinement Promotes Migration Through Dynamic Mode Reconfiguration. To determine how confinement alters migratory behavior, we built a quasi-3D migration system by overlaying a Matrigel layer on cells cultured on rigid substrates [Fig. 1(a)]. This configuration introduced an apical matrix boundary while preserving the basal interface with the rigid substrate.

Cells showed distinct protrusion morphologies and migratory behaviors under the two conditions. In the non-confined system, cells formed broad, wedge-shaped lamellipodia [Fig. 1(e)]. Under confinement, lamellipodia became laterally extended and markedly thinner [Fig. 1(f)]. Such changes are commonly observed when cells migrate in mechanically resistant matrix environments, where the shape of leading edges must adapt to increased matrix interaction [5,16,17]. Along with these morphological changes, cells in the confined condition explored larger distances [Figs. 1(c) and 1(d)], exhibiting higher mean squared displacements (MSD) [Fig. 1(b)] and migration speeds [Fig. 1(g)]. The diffusion exponent α, obtained from the slope of the log–log MSD curve, increased from approximately 1 in the non-confined condition to approximately 1.5 under confinement [Fig. 1(h)], indicating a shift from near-random motion to more persistent migration.

Cell area and volume were quantified based on three-dimensional reconstructions from confocal microscopy images. Cells revealed similar mean volume, spreading area, and surface area in the non-confined and confined conditions [Figs. 1(i) and 1(j), and Fig. S1(b) in the Supplementary Materials (SM)]. Thus, confinement increased migration without altering steady-state cell geometry. We then analyzed the fluctuations of single-cell surface area and volume during movement. In individual cells, both normalized volume (NV) and normalized surface area (NA) varied continuously over time [Figs. S1(h) and S1(i) in SM]. To allow comparison across cells and conditions, these quantities were normalized to their respective time-averaged values, accounting for cell-to-cell differences. The fluctuation ranges σ_{V} and σ_{A} were quantified from the full width at half maximum of the

Received 16 April 2026; accepted 11 May 2026; published 3 June 2026
© 2026 Chinese Physical Society and IOP Publishing Ltd. All rights, including for text and data mining, AI training, and similar technologies, are reserved.

Check for updates

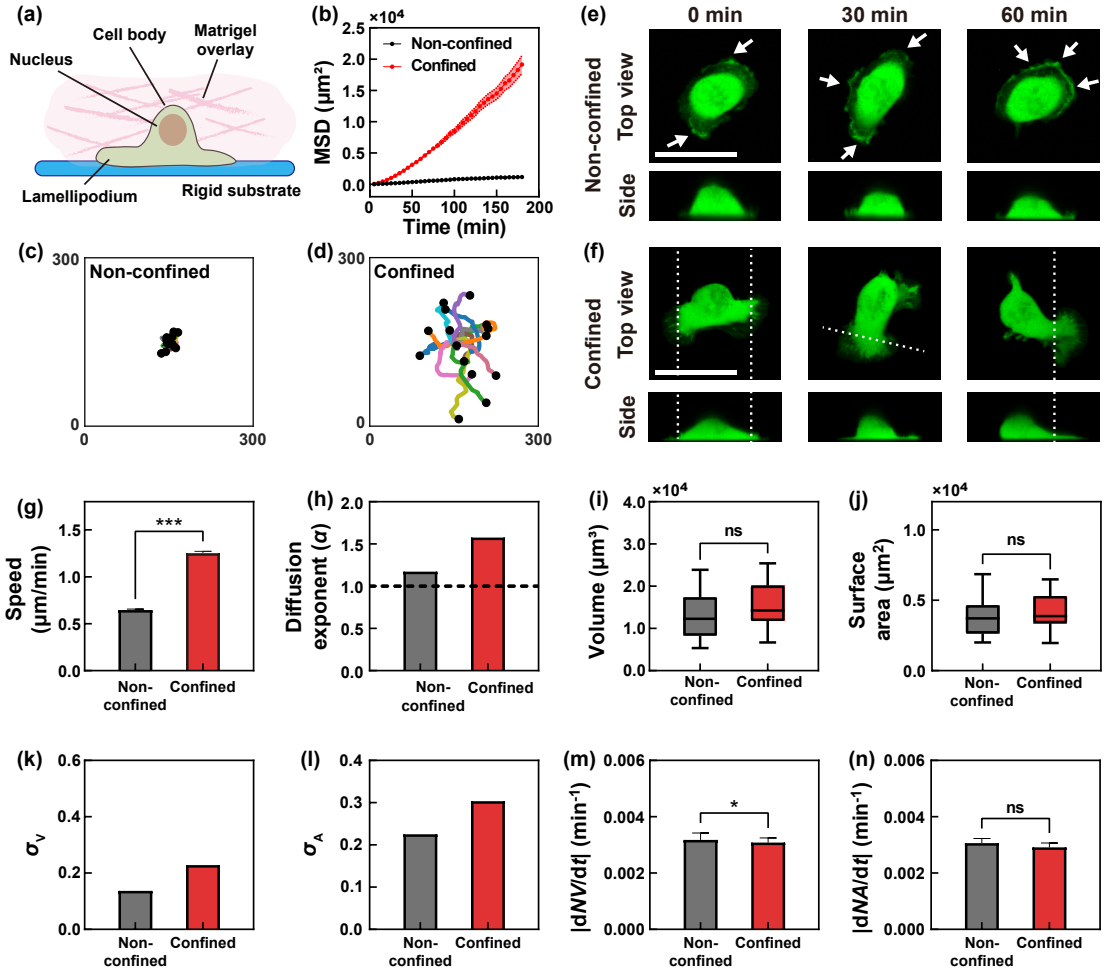

Fig. 1. Confinement enhances cell migration while preserving mean cell geometry. (a) Schematic of the quasi-3D cell–matrix model. (b) Mean squared displacement (MSD) over time (0–180 min) under the Non-confined and Confined conditions (Non-confined, $n = 507$; Confined, $n = 679$). Data points represent mean values, and error bars indicate SEM. (c) and (d) Representative migration trajectories of 15 cells over 145 min, with starting points aligned to a common origin, under the Non-confined (c) and Confined (d) conditions. (e) and (f) Representative three-dimensional confocal reconstructions of MDA-MB231-GFP cells under the Non-confined (e) and Confined (f) conditions. Arrowheads indicate wedge-shaped lamellipodia in the Non-confined condition, and dashed lines outline broad, thin lamellipodia in the Confined condition. Scale bar, 50 μm. (g) Cell migration speed under the Non-confined and Confined conditions (Non-confined, $n = 482$; Confined, $n = 653$). Bars represent mean ± SEM. Mann–Whitney test, $^{***}p < 0.001$. (h) Diffusion exponent α extracted from log–log MSD curves. The dashed line indicates $\alpha = 1$. (i) and (j) Box plots of cell volume (i) and surface area (j) under the Non-confined and Confined conditions (cell volume: Non-confined, $n = 32$; Confined, $n = 36$; surface area: Non-confined, $n = 29$; Confined, $n = 36$). Unpaired t-test, ns, not significant. (k) and (l) Fitted fluctuation amplitudes of volume σ_V (k) and surface area σ_A (l), defined as the full width at half maximum of the corresponding fitted distributions. (m) and (n) Rates of normalized volume change $|dNV/dt|$ (m) and normalized surface area change $|dNA/dt|$ (n) under the Non-confined and Confined conditions (Non-confined, 225 data points from $n = 32$; Confined, 223 data points from $n = 36$). Bars represent mean ± SEM. Mann–Whitney test, ns and $^{*}p < 0.05$.

corresponding distributions, and $|dNV/dt|$ and $|dNA/dt|$ were quantified from frame-to-frame changes (see SM). Under confinement, the fluctuation ranges of both cell volume and surface area increased [Figs. 1(k) and 1(l)], whereas the values of $|dNV/dt|$ and $|dNA/dt|$ differed only slightly between the two conditions [Figs. 1(m) and 1(n)]. Thus, the effect of confinement was more evident in the extent of volume–surface fluctuations than in mean cell geometry or fluctuation rate.

Confinement Alters Mechanical State and Weakens Volume–Surface Coupling. We next investigated whether spatial confinement modulated the cellular mechanical state. Quantitative analysis showed that cell height significantly decreased under confinement [Fig. 2(a)]. Furthermore, whereas the focal adhesion protein Vinculin was primarily restricted to the basal plane beneath the nucleus in unconfined cells, it localized to both the basal plane and the apical surface under confinement [Fig. 2(b)]. The mechanosensitive transcription factor YAP also exhibited increased nuclear accumulation in the confined condition [Figs. 2(c) and 2(d)].

We then quantified membrane tension using the Flipper-TR probe with fluorescence lifetime imaging microscopy (FLIM), where a longer lifetime indicates higher membrane tension [18]. Measurements were acquired at two focal planes: the apical plane, primarily sampling the membrane regions over the cell body, and the basal plane, enriched in lamellipodial membranes [Figs. 2(e) and 2(f)]. In unconfined cells, the basal plane exhibited longer lifetimes than the apical plane, indicating higher membrane tension in lamellipodial membrane regions. Under confinement, however, lifetimes increased significantly at the apical plane, reaching values slightly higher than those at the basal plane. This indicates a pronounced increase in membrane tension over the cell body. Thus, confinement alters the spatial distribution of membrane tension, effectively reducing the apical–basal tension gradient observed during unconfined migration. Together, these results indicate that confinement is accompanied by changes in multiple mechanical-state-related features of migrating cells.

We assessed volume–surface coordination using the dynamic correlation coefficient C, defined as the slope relating the normalized rates of volume change $|dNV/dt|$ and normalized surface area change

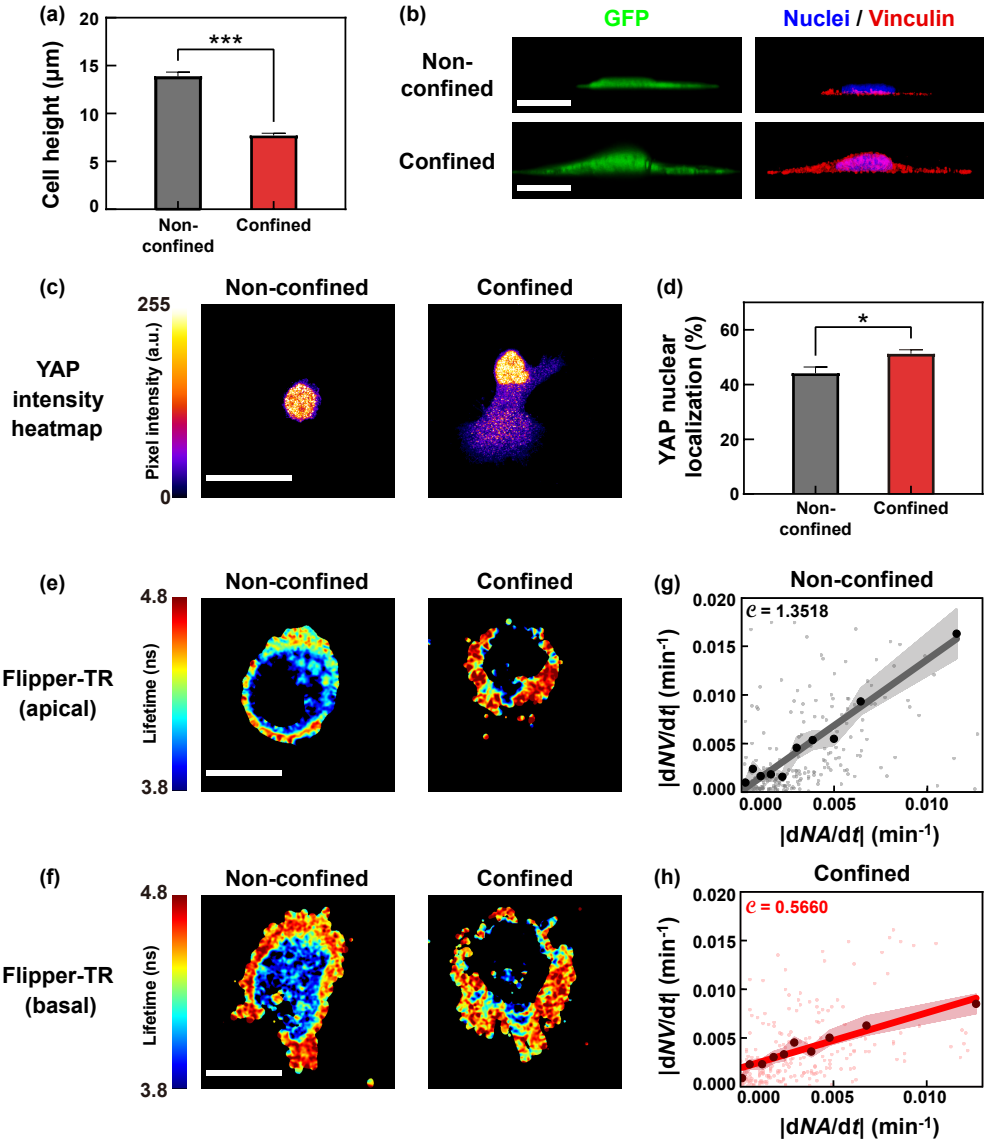

Fig. 2. Confinement alters mechanical state and weakens volume–surface coupling. (a) Cell height under the Non-confined and Confined conditions (Non-confined, $n = 21$; Confined, $n = 18$). Bars represent mean ± SEM. Welch's t-test, $^{***}p < 0.001$. (b) Representative side-view immunofluorescence images showing Vinculin distribution under the Non-confined (top) and Confined (bottom) conditions. Green, GFP; blue, nuclei (Hoechst); red, Vinculin. Scale bar, 20 μm. (c) Representative heatmaps of YAP immunofluorescence intensity in Fire LUT (0–255). Scale bar, 50 μm. (d) Quantification of YAP nuclear localization (Non-confined, $n = 11$; Confined, $n = 25$). Bars represent mean ± SEM. Unpaired t-test, $^{*}p < 0.05$. (e) and (f) Representative Flipper-TR FLIM images acquired at the apical plane (e) and basal plane (f) under the Non-confined (left) and Confined (right) conditions. Scale bar, 50 μm. The displayed lifetime ranges from 3.8 ns (blue) to 4.8 ns (red). (g) and (h) Scatter plots of $|\mathrm{d}NV/\mathrm{d}t|$ versus $|\mathrm{d}NA/\mathrm{d}t|$ under the Non-confined (g) and Confined (h) conditions. Sample sizes were Non-confined, 302 data points from $n = 32$, and Confined, 290 data points from $n = 36$.

$|\mathrm{d}NA/\mathrm{d}t|$ (see SM). We found that C decreased from 1.3518 in the non-confined condition to 0.5660 under confinement [Figs. 2(g) and 2(h)], indicating weaker volume–surface coupling in the confined migration state. Collectively, these results show that spatial confinement not only alters the mechanical state, but also weakens the coordination between volume regulation and surface remodeling.

Distinct Perturbations of Migration-Related Processes Converge on Increased C. Under confined conditions, cells migrated efficiently while maintaining a low dynamic correlation coefficient C. We next examined whether perturbing this migratory capacity would correspondingly alter C. To this end, we targeted two processes critical for confined migration: MMP-dependent matrix degradation [19] and myosin II-dependent actomyosin contractility [20]. Specifically, we used batimastat, a broad-spectrum matrix metalloproteinase (MMP) inhibitor, to suppress local matrix proteolysis during cell migration [21], and blebbistatin to reduce myosin II-dependent force generation [22]. All perturbations in this section were applied under the confined condition.

We first assessed the effects of MMP inhibition. Batimastat treatment reduced both migration distance and speed, accompanied by a modest decrease in the diffusion exponent α [Fig. S1(c) in SM, Figs. 3(d) and 3(l)]. Matrix displacement around the cell also decreased: the characteristic Matrigel displacement field at the leading edge was largely lost, and the remaining displacement was localized primarily above the cell body [Figs. 3(i) and 3(j)]. Interestingly, despite this impaired migration, treated cells still formed broad, thin lamellipodia similar to those of untreated cells [Figs. 3(a) and 3(b)]. At the same time, the volume fluctuation σ_{V} increased [Fig. 3(e)], while the surface fluctuation σ_{A} increased only slightly [Fig. 3(f)]. The normalized rates of change for both volume $|\mathrm{d}NV/\mathrm{d}t|$ and surface area $|\mathrm{d}NA/\mathrm{d}t|$ increased [Figs. 3(g) and 3(h)], indicating that cells maintained protrusive activity but failed to achieve effective forward

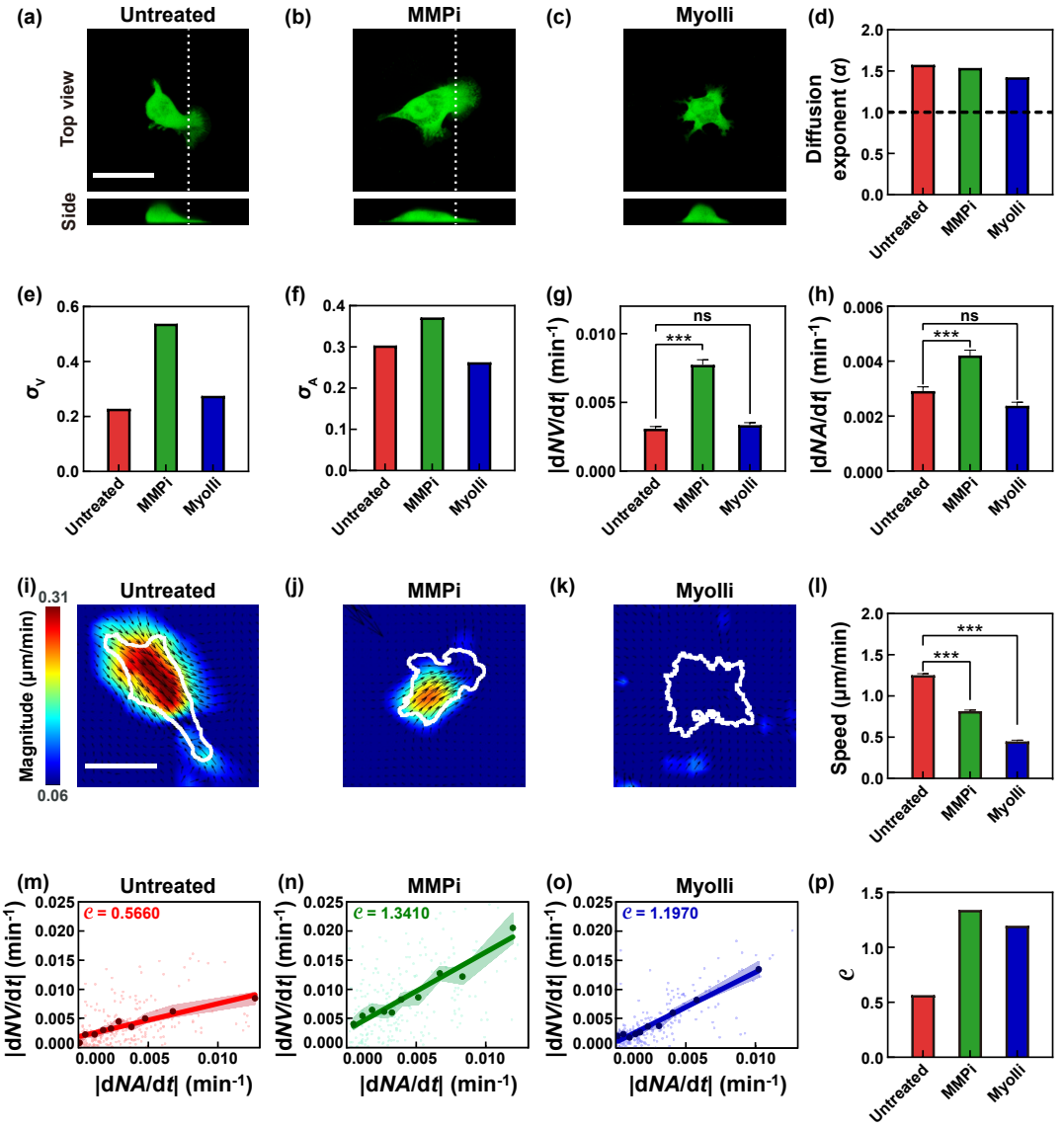

Fig. 3. Distinct perturbations of migration-related processes disrupt efficient migration and increase volume–surface coupling. (a)–(c) Representative 3D reconstructions of cells under the Confined condition without inhibitor treatment (a), after MMP inhibition (b), and after myosin II inhibition (c). Dashed lines delimit lamellipodia from the cell body. Scale bar, 50 μm. (d) Diffusion exponent α extracted from log–log MSD curves. The dashed line indicates $\alpha = 1$. The corresponding MSD curves are shown in Fig. S1 of the SM. (e) and (f) Fluctuation amplitudes of volume σ_V (e) and surface area σ_A (f) under the Untreated, MMPi, and MyoIIi conditions. (g) and (h) Rates of normalized volume change $|dNV/dt|$ (g) and normalized surface area change $|dNA/dt|$ (h). For $|dNV/dt|$: Untreated, 223 data points from $n = 36$; MMPi, 227 data points from $n = 39$; MyoIIi, 211 data points from $n = 27$. For $|dNA/dt|$: Untreated, 227 data points from $n = 36$; MMPi, 233 data points from $n = 39$; MyoIIi, 220 data points from $n = 27$. Bars represent mean ± SEM. Kruskal–Wallis test, ns and $^{***}p < 0.001$. (i)–(k) Particle image velocimetry (PIV) vector maps of matrix displacement. The color scale indicates displacement magnitude from 0.06 (blue) to 0.31 (red) μm/min. White solid lines indicate cell contours. Scale bar, 50 μm. (l) Cell migration speed (Untreated, $n = 653$; MMPi, $n = 590$; MyoIIi, $n = 234$). Bars represent mean ± SEM. Kruskal–Wallis test, $^{***}p < 0.001$. (m)–(o) Volume–surface dynamic correlation coefficient C under the Untreated (m), MMPi (n), and MyoIIi (o) conditions. Sample sizes were Untreated, 290 data points from $n = 36$; MMPi, 296 data points from $n = 39$; and MyoIIi, 265 data points from $n = 27$. (p) Comparison of C across the three conditions.

translocation.

Conversely, inhibition of myosin II with blebbistatin yielded a different morphological response, despite also reducing migration distance, speed, and the diffusion exponent α [Fig. S1(c) in SM, Figs. 3(d) and 3(l)]. Matrix displacement became even weaker, with no obvious deformation around the cells [Figs. 3(i) and 3(k)], indicating a severe reduction in mechanical coupling with the surrounding matrix. Unlike MMP inhibition, myosin II inhibition markedly reduced lamellipodial size [Figs. 3(a)–3(c)]. However, the fluctuation metrics of cell volume and surface area remained comparable to those of untreated cells [Figs. 3(e)–3(h)]. Thus, the two perturbations produced distinct dynamic signatures: MMP inhibition elevated the rates of volume and surface area changes, whereas myosin II inhibition primarily impaired lamellipodial extension and matrix deformation without appreciably altering volume or surface fluctuations.

Despite these distinct dynamic and morphological signatures, both perturbations increased the dynamic correlation coefficient C [MG: 0.5660, MMPi: 1.3410, MyoIIi: 1.1970; Figs. 3(m)–3(p)]. Together with the observed reduction in migration, these results indicate that impairing matrix degradation or reducing actomyosin contractility shifts cells away from the low-C dynamic state observed during efficient migration under confinement.

Distinct Perturbations of Volume Homeostasis Converge on Increased C. Because reduced migratory capacity under confinement was consistently accompanied by an increased C, we next asked whether perturbing volume homeostasis would produce a similar

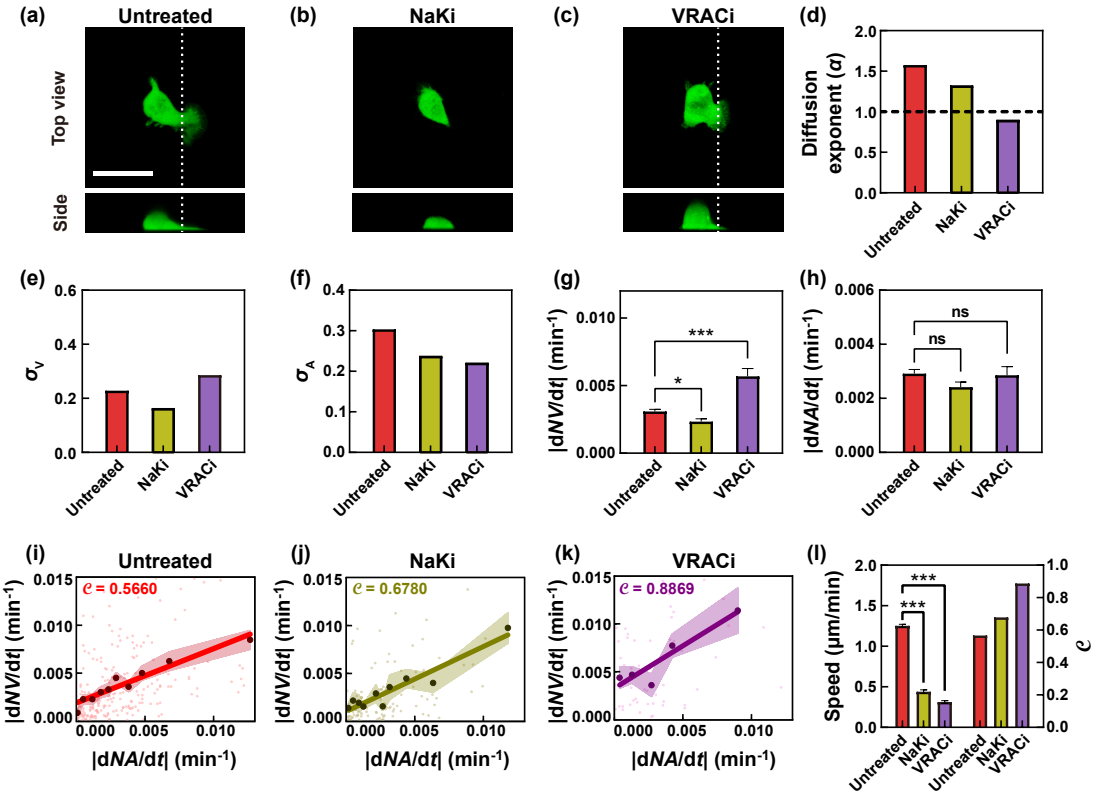

Fig. 4. Distinct perturbations of volume homeostasis disrupt efficient migration and increase volume–surface coupling. (a)–(c) Representative 3D reconstructions of cells under the Confined condition without inhibitor treatment (a), after Na^+/K^+-ATPase inhibition (b), and after VRAC inhibition (c). Dashed lines delimit lamellipodia from the cell body. Scale bar, 50 μm. (d) Diffusion exponent α extracted from log–log MSD curves. The dashed line indicates $\alpha = 1$. The corresponding MSD curves are shown in Fig. S1 of the SM. (e) and (f) Fluctuation amplitudes of volume σ_V (e) and surface area σ_A (f) under the Untreated, NaKi, and VRACi conditions. (g) and (h) Rates of normalized volume change $|dNV/dt|$ (g) and normalized surface area change $|dNA/dt|$ (h). For $|dNV/dt|$: Untreated, 223 data points from $n = 36$; NaKi, 104 data points from $n = 39$; VRACi, 54 data points from $n = 27$. For $|dNA/dt|$: Untreated, 227 data points from $n = 36$; NaKi, 103 data points from $n = 39$; VRACi, 52 data points from $n = 27$. Bars represent mean ± SEM. Kruskal–Wallis test, ns, $^*p < 0.05$, and $^{***}p < 0.001$. (i)–(k) Scatter plots of $|dNV/dt|$ versus $|dNA/dt|$ under the Untreated (i), NaKi (j), and VRACi (k) conditions, with fitted dynamic correlation coefficients C. Sample sizes were Untreated, 290 data points from $n = 36$; NaKi, 136 data points from $n = 22$; and VRACi, 62 data points from $n = 7$. (l) Dual-y-axis plot of cell migration speed (left y-axis) and C (right y-axis) under the three conditions. For speed: Untreated, $n = 653$; NaKi, $n = 73$; VRACi, $n = 95$. For C: Untreated, 290 data points from $n = 36$; NaKi, 136 data points from $n = 22$; VRACi, 62 data points from $n = 7$. Bars represent mean ± SEM. Kruskal–Wallis test, $^{***}p < 0.001$.

shift in this dynamic state. Volume regulation is critical for confined migration, where ion and water fluxes can facilitate sustained deformation [3,23]. We inhibited the Na^+/K^+-ATPase, which maintains the ion gradients required for long-term volume stability, using ouabain [14]. The volume-regulated anion channel (VRAC), which supports regulatory volume decrease and cell volume recovery after swelling [24], was perturbed with mefloquine [25]. All perturbations in this section were also applied under the confined condition.

Both perturbations reduced cell migration. Compared with untreated cells, those subjected to either inhibitor exhibited lower MSD amplitudes [Fig. S1(d) in SM], decreased migration speeds [Fig. 4(l)], and reduced diffusion exponents α [Fig. 4(d)]. Furthermore, representative 3D reconstructions revealed that both treatments resulted in smaller and narrower lamellipodia [Figs. 4(a)–4(c)]. However, the two perturbations differed in their effects on fluctuation-related parameters [Figs. 4(e)–4(h)]. Following Na^+/K^+-ATPase inhibition, both σ_V and σ_A decreased [Figs. 4(e) and 4(f)]. In contrast, VRAC inhibition increased σ_V and $|dNV/dt|$ [Figs. 4(e) and 4(g)], while reducing σ_A [Fig. 4(f)]. Thus, the two treatments affected volume dynamics differently: Na^+/K^+-ATPase inhibition was accompanied by reduced fluctuation ranges, whereas VRAC inhibition was associated with broader volume fluctuations. Despite these distinct responses, both perturbations ultimately increased the dynamic correlation coefficient C [MG: 0.5660, NaKi: 0.6780, VRACi: 0.8869; Figs. 4(i)–4(l)]. Coupled with the observed defects in motility, these results suggest that perturbation of volume homeostasis is accompanied by a shift away from the low-C dynamic state associated with efficient migration under confinement.

Discussion

Cancer cell migration through matrix-rich environments is a critical step in metastasis [16]. During productive migration, cells continuously remodel and deform their boundaries through protrusion, adhesion, and contraction [26,27]. Here, we show that the quasi-3D Matrigel-induced confined culture environment significantly alters cell morphology and is accompanied by enhanced migration speed and persistence (Fig. 1). Because changes in mean cell geometry were insufficient to explain confinement-enhanced migration [Fig. 1(i), Fig. 1(j), and Fig. S1(b) in SM], we introduced a volume–surface dynamic correlation coefficient, C, to quantify the dynamic relationship between volume regulation and surface remodeling during migration.

Under confinement, C decreases significantly [Figs. 2(g) and 2(h)]. A smaller C indicates weaker immediate coupling between volume regulation and surface remodeling. One physical interpretation is that surface remodeling first changes the mechanical load borne by the membrane–cortex system, and volume regulation then responds through mechano-osmotic processes with a finite delay. This interpretation is supported by the mechano-osmotic feedback model of Venkova *et al.*, in which cell deformation rate, membrane tension, cortical mechanics, and ion fluxes jointly set volume changes [9]. Thus, surface remodeling and volume regulation do not need to occur

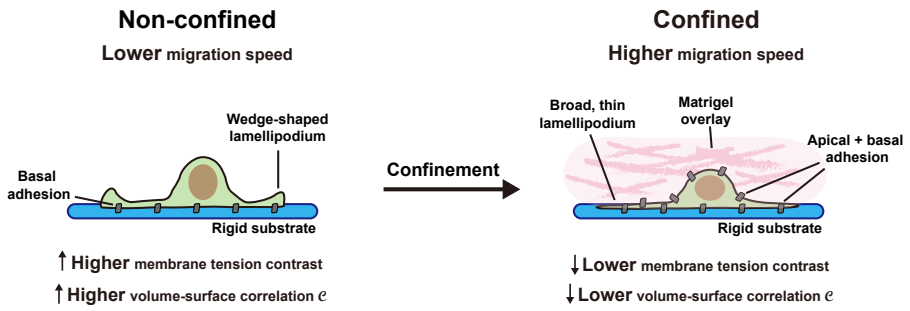

Fig. 5. Schematic summary of confinement-associated changes in migration and volume–surface coupling. Under the Non-confined condition, cells display wedge-shaped lamellipodia, predominantly basal adhesion, higher membrane tension contrast, higher volume–surface dynamic correlation coefficient C, and lower migration speed. Under the Confined condition, the Matrigel overlay introduces an apical matrix boundary, and cells form broad, thin lamellipodia with adhesion redistributed to both apical and basal surfaces. This confined state is accompanied by lower membrane tension contrast, lower C, and higher migration speed.

in a strictly synchronous manner. Based on this framework, C would be expected to increase when surface remodeling generates stronger membrane–cortex load, or when this load relaxes more slowly through the membrane–cortex system. Conversely, volume regulation mediated by ion and water fluxes may allow cells to accommodate surface changes with less immediate volume adjustment, thereby contributing to a lower C.

The reduced C under confinement is likely linked to the participation of the apical interface in force transmission. The Matrigel overlay introduces an apical matrix boundary above the basal adhesive interface [Fig. 1(a)]. Under this condition, Vinculin was no longer restricted to the basal plane but was also detected near the apical interface, together with increased nuclear YAP [Figs. 2(b)–2(d)]. Meanwhile, the increased apical Flipper-TR lifetime and the reduced apical–basal contrast suggest that the apical membrane becomes more mechanically involved under confinement [Figs. 2(e) and 2(f)]. These observations suggest that the apical boundary is mechanically engaged during confined migration, allowing mechanical load associated with surface remodeling to be shared across apical and basal interfaces [7]. This redistribution may reduce local membrane-tension buildup, thereby making surface remodeling less immediately coupled to volume regulation [10] and contributing to the reduced C (Fig. 5).

The relation between C and motility can be understood from the cost of surface remodeling during migration [7]. When C is low, surface remodeling requires less immediate adjustment of cell volume, reducing the mechanical and osmotic cost of sustained boundary deformation [9,10]. This state is therefore more compatible with sustained cell migration. A higher C indicates tighter coupling between surface remodeling and volume regulation, which can increase the coordination cost of migration and reduce motility [3,4].

Perturbation experiments further support this interpretation. MMP inhibition limits extracellular matrix degradation and local matrix remodeling [17,19], which may increase the matrix resistance encountered during surface remodeling. This increased resistance may strengthen the mechanical load transmitted to the membrane–cortex system, contributing to the increased C. Myosin II inhibition lowers cortical contractility [20,22] and may slow the relaxation of membrane–cortex load during boundary deformation. As a result, volume regulation would become more tightly coupled to surface remodeling. Na^+/K^+-ATPase inhibition and VRAC inhibition directly perturb ion- and water-mediated volume regulation by disrupting osmotic balance and impairing regulatory volume decrease, respectively [14,24,25]. When volume homeostasis is compromised, surface-area fluctuations are more directly translated into whole-cell volume changes due to weakened osmotic feedback regulation, leading to an elevated C. Although these four interventions altered cell geometry and deformation dynamics differently, they converged on increased C and reduced motility (Figs. 3 and 4). This shared change further supports the association between weak volume–surface coupling and efficient migration under confinement.

In addition to altered volume–surface coordination, confinement was accompanied by a leading-edge transition from a thicker wedge-shaped protrusion to a broader and thinner lamellipodium [Figs. 1(e) and 1(f)]. This change indicates that the protrusive front is reorganized during confined migration. This structural reorganization is consistent with evidence that lamellipodial shape governs migration speed [28] and migration-mode switching [29].

While our quasi-3D model is not a fully embedded 3D environment, it captures an interface-associated confinement relevant to basement membranes and vascular walls. We demonstrate that an apical boundary modulates the biophysical properties of migrating cells. Related volume-dependent physical changes have also been observed in a 3D environment, where cells at the less-stressed invasive front of breast cancer organoids undergo swelling and softening [30]. These findings suggest that tumor cells may use volume regulation to adapt to spatial confinement, including in complex three-dimensional environments. Consequently, the volume-dependent adaptations identified here may be relevant to broader 3D invasion contexts. This study focuses on MDA-MB231 breast cancer cells, and whether similar mechanical plasticity occurs in other invasive malignancies or non-malignant epithelial cells requires further investigation. Nevertheless, this quantitative framework offers a perspective on how invasive cells mechanically adapt to complex 3D microenvironments.

Author Contributions

F.Y., Q.F., and X.W. conceived the research. M.X., B.S. and X.W. designed and carried out the experiments. All authors analyzed the data and wrote the paper.

Acknowledgements

We thank Heyang Zhang, Dingchen Kang, Zihao Yu, Dingchao Rong, and Yipu Wang for their diligent assistance with long-term time-lapse microscopy during a three-week summer research internship. We thank Yongliang Zhai for the design and fabrication of a homemade live-cell incubating system. This work was supported by the National Key Research and Development Program of China (Grant No. 2022YFA1405002), the National Natural Science Foundation of China (Grant Nos. 12325405, 12422408, T2221001, 12434008, and 12304253), and the Zhejiang Provincial Natural Science Foundation of China (Grant No. LQ24A040013).

References

[1] Chaudhuri O, Cooper-White J, Janmey P A, Mooney D J, and Shenoy V B 2020 *Nature* **584** 535
[2] Pally D and Naba A 2024 *Curr. Opin. Cell Biol.* **86** 102309
[3] Stroka K M, Jiang H, Chen S H, Tong Z, Wirtz D, Sun S X, and Konstantopoulos K 2014 *Cell* **157** 611
[4] Morishita K, Watanabe K, and Ichijo H 2019 *Cancer Sci.* **110** 2337
[5] Doyle A D, Sykora D J, Pacheco G G, Kutys M L, and Yamada K M

2021 *Dev. Cell* **56** 826
[6] Yamada K M, Doyle A D, and Lu J 2022 *Trends Cell Biol.* **32** 883
[7] De Belly H, Yan S, Borja da Rocha H, Ichbiah S, Town J P, Zager P J, Estrada D C, Meyer K, Turlier H, Bustamante C, and Weiner O D 2023 *Cell* **186** 3049
[8] Bodor D L, Pönisch W, Endres R G, and Paluch E K 2020 *Dev. Cell* **52** 550
[9] Venkova L, Vishen A S, Lembo S, Srivastava N, Duchamp B, Ruppel A, Williart A, Vassilopoulos S, Deslys A, Garcia Arcos J M, Diz-Muñnoz A, Balland M, Joanny J F, Cuvelier D, Sens P, and Piel M 2022 *eLife* **11** e72381
[10] Roffay C, Molinard G, Kim K, Urbanska M, Andrade V, Barbarasa V, Nowak P, Mercier V, García-Calvo J, Matile S, Loewith R, Echard A, Guck J, Lenz M, and Roux A 2021 *Proc. Natl. Acad. Sci. U.S.A.* **118** e2103228118
[11] Xie J, Huck W T S, and Bao M 2024 *Annu. Rev. Biophys.* **53** 299
[12] Guo M, Pegoraro A F, Mao A, Zhou E H, Arany P R, Han Y, Burnette D T, Jensen M H, Kasza K E, Moore J R, Mackintosh F C, Fredberg J J, Mooney D J, Lippincott-Schwartz J, and Weitz D A 2017 *Proc. Natl. Acad. Sci. U.S.A.* **114** E8618
[13] Adar R M and Safran S A 2020 *Proc. Natl. Acad. Sci. U.S.A.* **117** 5604
[14] Hoffmann E K, Lambert I H, and Pedersen S F 2009 *Physiol. Rev.* **89** 193
[15] Driscoll M K and Danuser G 2015 *Trends Cell Biol.* **25** 749
[16] Friedl P and Alexander S 2011 *Cell* **147** 992
[17] Wolf K, Te Lindert M, Krause M, Alexander S, Te Riet J, Willis A L, Hoffman R M, Figdor C G, Weiss S J, and Friedl P 2013 *J. Cell Biol.* **201** 1069
[18] Colom A, Derivery E, Soleimanpour S, Tomba C, Molin M D, Sakai N, González-Gaitán M, Matile S, and Roux A 2018 *Nat. Chem.* **10** 1118
[19] Sabeh F, Ota I, Holmbeck K, Birkedal-Hansen H, Soloway P, Balbin M, López-Otín C, Shapiro S, Inada M, Krane S, Allen E, Chung D, and Weiss S J 2004 *J. Cell Biol.* **167** 769
[20] Cowan J M, Duggan J J, Hewitt B R, and Petrie R J 2022 *Front. Cell Dev. Biol.* **10** 1047256
[21] Hotary K, Allen E, Punturieri A, Yana I, and Weiss S J 2000 *J. Cell Biol.* **149** 1309
[22] Limouze J, Straight A F, Mitchison T, and Sellers J R 2004 *J. Muscle Res. Cell Motil.* **25** 337
[23] Zhang Y, Li Y, Thompson K N, Stoletov K, Yuan Q, Bera K, Lee S J, Zhao R, Kiepas A, Wang Y, Mistriotis P, Serra S A, Lewis J D, Valverde M A, Martin S S, Sun S X, and Konstantopoulos K 2022 *Nat. Commun.* **13** 6128
[24] Osei-Owusu J, Yang J, Vitery M d C, and Qiu Z 2018 *Curr. Top. Membr.* **81** 177
[25] Maertens C, Wei L, Droogmans G, and Nilius B 2000 *J. Pharmacol. Exp. Ther.* **295** 29
[26] Gardel M L, Schneider I C, Aratyn-Schaus Y, and Waterman C M 2010 *Annu. Rev. Cell Dev. Biol.* **26** 315
[27] Ridley A J, Schwartz M A, Burridge K, Firtel R A, Ginsberg M H, Borisy G, Parsons J T, and Horwitz A R 2003 *Science* **302** 1704
[28] Ofer N, Mogilner A, and Keren K 2011 *Proc. Natl. Acad. Sci. U.S.A.* **108** 20394
[29] Jiang C, Luo H Y, Xu X, Dou S X, Li W, Guan D, Ye F, Chen X, Guo M, Wang P Y, and Li H 2023 *Nat. Commun.* **14** 5166
[30] Han Y L, Pegoraro A F, Li H, Li K, Yuan Y, Xu G, Gu Z, Sun J, Hao Y, Gupta S K, Li Y, Tang W, Tang X, Teng L, Fredberg J J, and Guo M 2020 *Nat. Phys.* **16** 101